ELSEVIER

Journal of Fluids and Structures 19 (2004) 713–727

JOURNAL OF FLUIDS AND STRUCTURES

www.elsevier.nl/locate/jnlabr/yjfls

Comparison of experiments and reduced-order models for turbomachinery high-incidence flutter

G.S. Copeland[a,*], G.J. Rey[b]

[a] *United Technologies Research Center, MS129-65, 411 Silver Lane, East Hartford, CT 06108, USA*
[b] *Pratt and Whitney Aircraft Engines, MS 182-94, 400 Main Street, East Hartford, CT 06108, USA*

Received 19 September 2003; accepted 28 January 2004

Abstract

Experimental data and analyses of a reduced-order model are compared. The model is based on simplified physics (actuator disk modelling of bladerows, typical section aeroelastic model) and the measured steady performance characteristic. The model is not intended to be predictive, though it has been shown to be "tunable" to stability measurements of the test rig. The objective of the effort is to estimate the relative sensitivity of flutter damping to system parameters. It is found that flutter damping and stability predictions are in good quantitative agreement with measured test rig data and industry experience. It is shown that the correct trends are predicted for alternate stiffness and stagger mistuning.

Keywords: Aeroelasticity; Aeromechanics; Flutter; Turbomachinery; Mistuning

1. Introduction

Experimental flutter stability data acquired on a laboratory-scale fan research facility have been compared to the results from a previously developed reduced-order model (Copeland and Rey 1998). The compressor characteristic was empirically determined from measurements and model parameters describing total pressure loss across each bladerow were chosen to match those measurements. Trends in damping and stability of high-incidence flutter with shaft speed and mass flow were predicted in good agreement with the measurements.

The reduced-order model for simulation and stability analysis of high-incidence flutter and rotating stall was constructed based on an actuator disk approach. The analytical description is based on matching two-dimensional incompressible flow fields across actuator disks representing a flexible rotor and a rigid stator. The model takes the form of a system of differential-algebraic equations derived from idealized governing equations using symbolic algebra. The framework is such that changes to the physical modelling can be easily incorporated.

The fundamental difference between the present actuator disk modelling approach and the classical methods (Whitehead 1987) is that there is no attempt here to model the flow in the blade passages. It is assumed that the blade geometry largely determines the flow angles and that the pressure rise across each bladerow can be experimentally measured. The aerodynamic force on the flexible blades can then be determined directly using the control volume approach.

*Corresponding author. Tel.: +1-860-610-7453; fax: +1-860-660-1074.
E-mail address: copelags@utrc.utc.com (G.S. Copeland).

0889-9746/$ - see front matter © 2004 Elsevier Ltd. All rights reserved.
doi:10.1016/j.jfluidstructs.2004.01.008

Reduced-order models may be appropriate for on-engine diagnostics and control. The present model has been used to support experimental work in diagnostics and control (Banaszuk et al. 2002). They may also be used to test some of the simplifications typically necessary in higher-fidelity computational models such as the modelling of losses, choice of the inlet boundary condition, and the influence of downstream bladerows. One cannot expect good predictive capability from such a model; rather the objective is to determine qualitatively the trends in system stability and nonlinear dynamics as system parameters are varied. The focus of the present work is on the determination of stability boundaries through generalized eigensystem analyses and their parametric sensitivity. Numerical simulation and analysis have been used previously to demonstrate that stable flutter and stall limit cycles may coexist (Copeland 1997).

2. Experiment

Measurements of flutter damping were conducted on the 17″-fan test rig shown in Fig. 1. The rig has one fan stage with 16 blades on a rotor powered by an external air turbine and one (stator) row of exit guide vanes. The titanium rotor blades are found to flutter in their first bending mode of vibration. The rotor-frame frequency of this mode increases with shaft speed due to centrifugal stiffening; the in-vacuum natural frequency of vibration is predicted with finite-element modelling to be 242 Hz at 9000 r.p.m. There is a much smaller aerodynamic effect on stiffness. Varying the fan exit area with a translating throttle plug controls the flow through the rig. Reducing the throttle area decreases the flow, which increases the incidence angle of the air approaching the blades ultimately de-stabilizing the flutter modes.

The methodology for aeromechanical system identification is shown in Fig. 2. Two eddy current sensors were used independently to measure the blade displacement in the stationary frame. Passage of a blade results in an impulse in the signal from the eddy current sensors. The time difference DT between the measured arrival time and the "rigid-blade" arrival time (based on the shaft speed and the number of blades) was used as a measure of blade deflection. Ten speakers mounted in cavities evenly distributed around the fan casing were used as actuators. The experiments reported here were performed at 8000, 8500, 9000, and 9500 r.p.m. at multiple throttle settings for each speed.

A well-known characteristic of turbomachinery flutter is the frequency distribution of the flutter modes as measured in the stationary frame. A forward-travelling flutter mode

$$\alpha(\theta, t), q(\theta, t) \propto \exp(\omega t - n\theta)$$

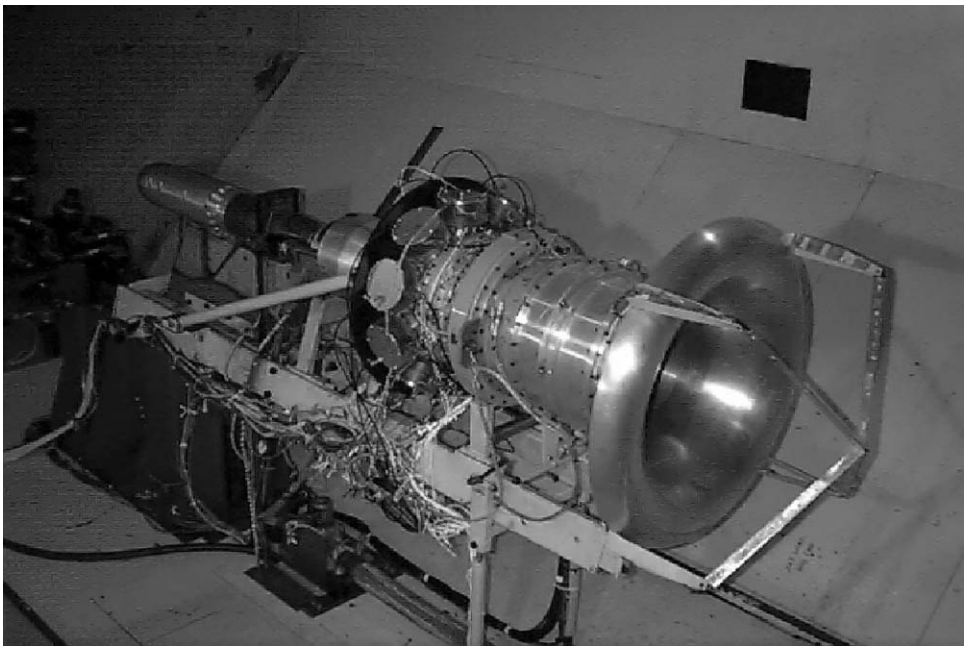

Fig. 1. 17″ diameter experimental fan rig.

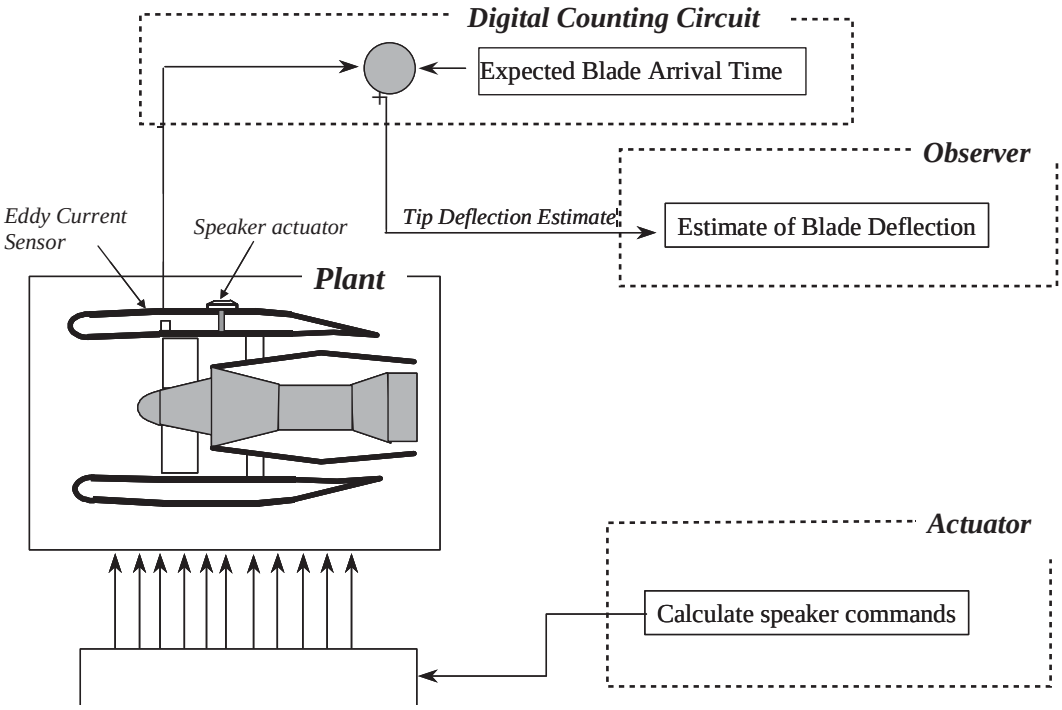

Fig. 2. Schematic of off-blade aeromechanical identification system.

will have an observed stator frame frequency equal to

$$\omega_{+n} = \omega + n\Omega,$$

where Ω is the angular velocity of the rotor shaft.

For system identification the flutter modes were modelled as a real-valued second-order system. The parameters were identified from swept-sine experiments. A second-order transfer function was fitted to the experimentally obtained transfer function from a spectral analyzer. The actuators were used to drive a standing wave in the form of a discretized cosine. For example, speaker m, where m is between 1 and 10, was driven with an excitation signal

$$f_m(t) = f_0 \cos\left(2\pi \frac{m}{10}\right)\cos(\omega t).$$

Fig. 3 shows the Bode plots from a sine-sweep experiment and the corresponding second-order fits for flutter modes for nodal diameter $n = 2$ at 9000 r.p.m. and a mass flow rate of 39 lbm/s. Note that the second-order transfer function fits to experimental data are good near the flutter frequency (i.e., the frequency at the resonant peak of the magnitude), but there is an increasing phase error away from the flutter frequency. The measured stationary-frame flutter frequency is 552 Hz corresponding to a rotor frame frequency of 252 Hz. The measured rotor-frame damping ratio is 0.0070.

3. Mathematical model

Modelling for flutter prediction has been shown to be a difficult technical challenge even for computational fluid dynamics approaches [Silkowski *et al.* (2002)] with a high-fidelity representation of the fundamental physics. It is reasonable to question why a simple actuator-disk approach should work. System stability is determined fundamentally by the balance of mass, momentum, and energy across each element of the system. The effects that are hardest to predict from first principles are exactly those that are determined empirically in the present approach.

Limitations of the present approach include:

(i) typical-section airfoil only appropriate for low-order structural modes—a reasonable assumption for high-incidence flutter;

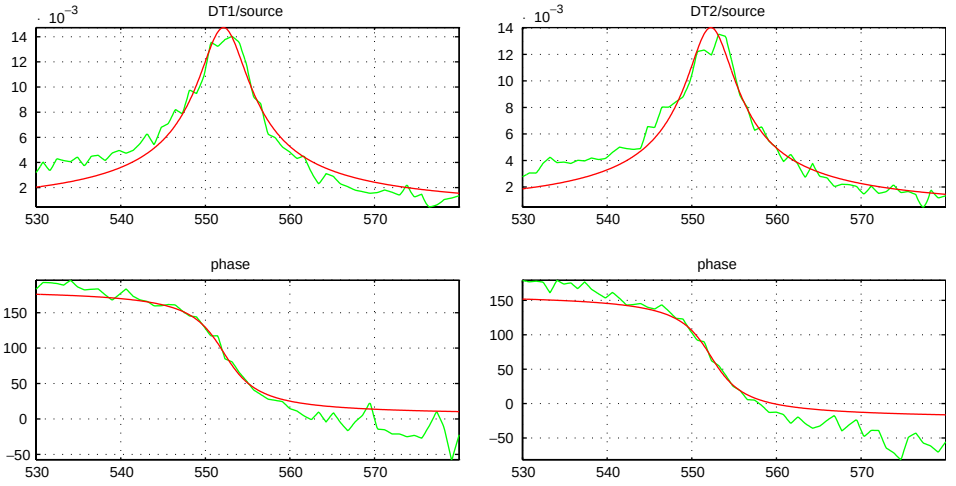

Fig. 3. Transfer functions for flutter mode $n=2$. Experimental data and second-order fit.

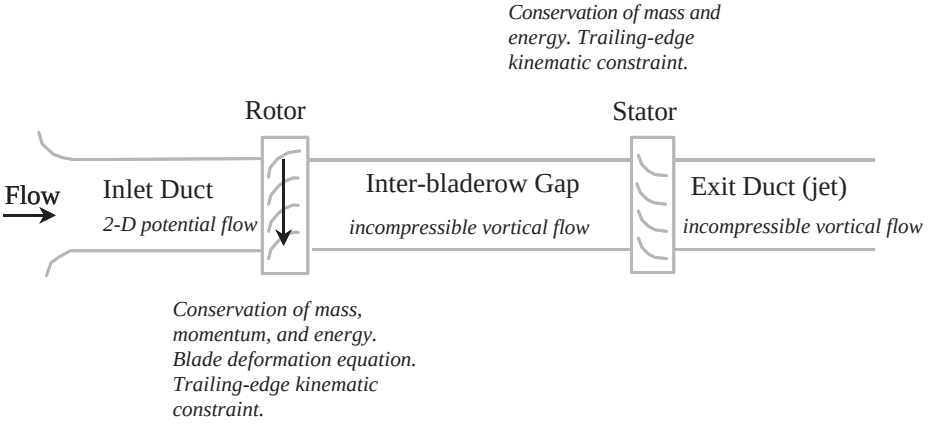

Fig. 4. Physical schematic.

(ii) there is no accounting for structural coupling between blades—this coupling is particularly important for shrouded fans and integrally bladed rotors;
(iii) actuator disk implies a continuum of blades; flow perturbations that are comparable in scale to the blade-passage width may not be captured well by empirical approximations for loss or by modelled physics;
(iv) losses depend on secondary flows (three dimensional); empirical functions for loss do not extrapolate well;
(v) the aerodynamic center is assumed fixed; in reality, it is of course a function of the flow and may vary considerably as the flow becomes trans-sonic.

A schematic of the physical model is shown in Fig. 4. The fundamental variables governing the flow are the components of velocity and pressure at four discrete axial stations: the rotor leading edge (1),[1] the rotor trailing edge (2a), the stator leading edge (2b), and the stator trailing edge (3). At each station, equations are derived relating the flow variables at that station to the flow variables at the previous station (or the free stream). Additional variables are required to account for dynamic losses, rotor deformation, and vorticity transport. The dynamic equations associated with the rotor actuator disk relating the flow variables at the rotor trailing edge to the flow at the rotor leading edge

[1] These numbers correspond to the subscripts used in the symbols, in the analysis that follows.

require additional states describing blade deformation and total pressure loss. The equations associated with the inter-bladerow gap relating the flow variables at the stator leading edge to the flow variables at the rotor trailing edge require additional variables describing the vorticity field. The exit guide vanes are assumed rigid but additional variables for dynamic loss across the stator are required.

The underlying physics and assumptions for the each of the model components are described below. For brevity, the derivation of the underlying differential-algebraic equations of the model is discussed for the rotating bladerow only. These are the most complicated equations of the model and the approach taken differs significantly from previous investigators. Full details of the development of the model equations are described in Copeland and Rey (1998).

3.1. Inlet duct

Modelling of the flow in the inlet duct is identical to that of Moore and Greitzer (1986). The azimuthal dependence of the flow is modelled by a linear perturbation to the nominal axisymmetric flow. The perturbation flow field is assumed to be irrotational and incompressible. The system is assumed to draw flow from a reservoir with constant total pressure, which would include the relative free-stream velocity. The governing equations are the conservation of mass and momentum.

3.2. Rotor

As mentioned previously, we do not attempt to model the flow in the blade passage; rather it is treated as a control volume. The actuator disk equations relate the flow velocity components and pressure at the upstream face ϕ_1, v_1, and p_1, to the velocity components and pressure at the downstream face ϕ_{2a}, v_{2a}, and p_{2a}. These are derived from the conservation equations for mass, momentum, and energy in the deforming control volume. The equations for blade vibration and a kinematic constraint on the trailing-edge flow velocity are also required for closure.

In contrast to the Gysling and Myers (1996) and Wong (1997), all flow and blade deformation quantities are determined as smoothly varying functions of the azimuthal angle. In those earlier works, a representative blade passage was taken as the control volume. In the present approach the control volume can be taken arbitrarily thin, which is more consistent with an actuator disk approach.

3.2.1. Conservation of mass

Conservation of mass within the deforming control volume may be expressed as follows:

$$\frac{\mathrm{d}}{\mathrm{d}t}\int \rho \,\mathrm{d}V + \int \rho(\boldsymbol{v}_r \cdot \boldsymbol{n})\,\mathrm{d}S = 0.$$

The subscript r on the velocity vector indicates velocity with respect to the moving boundary. The time derivate on the volume integral is to be taken in the rotor frame. The flow is assumed to be two dimensional and incompressible. Mass flux occurs over the leading- and trailing-edge boundaries only, hence the mass conservation equation may be expressed

$$\left(\frac{\partial}{\partial t} - \frac{\partial}{\partial \theta}\right)\frac{\partial V}{\partial \theta} + (\boldsymbol{v}_{r,le} \cdot \boldsymbol{n}_{le})\frac{\partial s_{le}}{\partial \theta} + (\boldsymbol{v}_{r,te} \cdot \boldsymbol{n}_{te})\frac{\partial s_{te}}{\partial \theta} = 0, \tag{1}$$

where the gradient of the volume is approximated by

$$\frac{\partial V}{\partial \theta} = c\cos(\gamma_r - \alpha)\frac{1}{2}\left(\frac{\partial s_{te}}{\partial \theta} + \frac{\partial s_{le}}{\partial \theta}\right),$$

s_{te} and s_{le} are path lengths along the leading- and trailing-edge boundaries of the control volume,

$$\frac{\partial s_{le}}{\partial \theta} = \sqrt{\left(\frac{\partial x_{le}}{\partial \theta}\right)^2 + \left(\frac{\partial \theta_{le}}{\partial \theta}\right)^2}, \quad \frac{\partial s_{te}}{\partial \theta} = \sqrt{\left(\frac{\partial x_{te}}{\partial \theta}\right)^2 + \left(\frac{\partial \theta_{te}}{\partial \theta}\right)^2},$$

and x_{le}, θ_{le}, x_{te}, and θ_{te} are coordinates of the leading and trailing edges of the control volume,

$$\theta_{le} = \theta + q\cos\gamma_r - \xi_{ea}c\sin(\gamma_r - \alpha), \quad \theta_{te} = \theta + q\cos\gamma_r + (1 - \xi_{ea})c\sin(\gamma_r - \alpha),$$
$$x_{le} = -q\sin\gamma_r - \xi_{ea}c\cos(\gamma_r - \alpha), \quad x_{te} = -q\sin\gamma_r + (1 - \xi_{ea})c\cos(\gamma_r - \alpha).$$

The relative velocity between the flow and the control volume leading edge is given by

$$\boldsymbol{v}_{r,le} = (\phi_1 \boldsymbol{i} + v_1 \boldsymbol{j}) - \left(\frac{\partial}{\partial t} - \frac{\partial}{\partial \theta}\right)(x_{le}\boldsymbol{i} + \theta_{le}\boldsymbol{j}).$$

Similarly, the relative velocity between the flow and the control volume trailing edge is given by

$$\boldsymbol{v}_{r,te} = (\phi_{2a} \boldsymbol{i} + v_{2a} \boldsymbol{j}) - \left(\frac{\partial}{\partial t} - \frac{\partial}{\partial \theta}\right)(x_{te}\boldsymbol{i} + \theta_{te}\boldsymbol{j}).$$

The outward normal vectors are given by

$$\boldsymbol{n}_{le} = -\cos\beta_{le}\boldsymbol{i} + \sin\beta_{le}\boldsymbol{j}, \quad \boldsymbol{n}_{te} = \cos\beta_{te}\boldsymbol{i} - \sin\beta_{te}\boldsymbol{j},$$

where the angles β_{le} and β_{te} are given by

$$\tan\beta_{le} = \frac{\partial x_{le}/\partial\theta}{\partial\theta_{le}/\partial\theta}, \quad \tan\beta_{te} = \frac{\partial x_{te}/\partial\theta}{\partial\theta_{te}/\partial\theta}.$$

The control volume definition sketch and the positive sense of blade deformation are shown in Fig. 5.

3.2.2. Conservation of linear momentum

For two-dimensional incompressible flow with mass flux through the leading- and trailing-edge boundaries, conservation of linear momentum within the deforming control volume may be expressed as

$$\left(\frac{\partial}{\partial t} - \frac{\partial}{\partial \theta}\right)\left(\boldsymbol{v}\frac{\partial V}{\partial \theta}\right) + [\boldsymbol{v}_{le}(\boldsymbol{v}_{r,le}\cdot\boldsymbol{n}_{le}) + p_{le}\boldsymbol{n}_{le}]\frac{\partial s_{le}}{\partial\theta} + [\boldsymbol{v}_{te}(\boldsymbol{v}_{r,te}\cdot\boldsymbol{n}_{te}) + p_{te}\boldsymbol{n}_{te}]\frac{\partial s_{te}}{\partial\theta} = -\frac{\partial \boldsymbol{F}}{\partial\theta}, \tag{2}$$

where $\boldsymbol{F}$ is the force exerted on the flow by the blades. The rotor-frame leading- and trailing-edge flow velocities and pressures are given by

$$\boldsymbol{v}_{le} = \phi_1\boldsymbol{i} + (1 + v_1)\boldsymbol{j}, \quad \boldsymbol{v}_{te} = \phi_{2a}\boldsymbol{i} + (1 + v_{2a})\boldsymbol{j},$$

$$p_{le} = p_1, \quad p_{te} = p_{2a}.$$

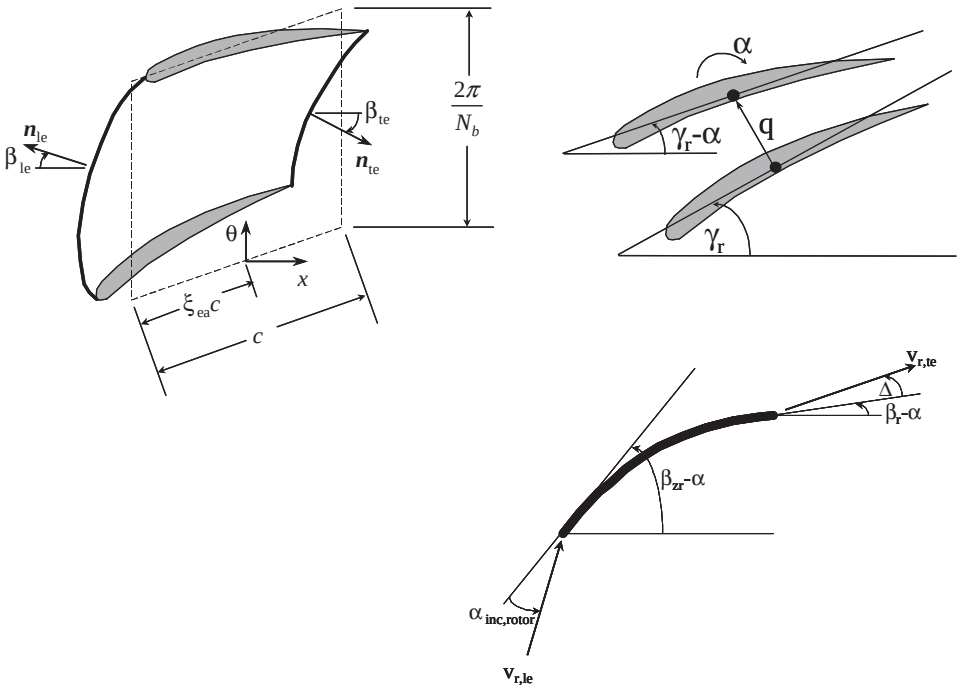

Fig. 5. Definition sketch for blade passage control volume (left), blade deflection (upper right), and flow geometry (lower right). The location of the elastic axis is indicated by the circle.

Additionally, the flow velocity within the control volume is approximated by the average of the leading- and trailing-edge flow velocities

$$\boldsymbol{v} = \tfrac{1}{2}(\boldsymbol{v}_{le} + \boldsymbol{v}_{te}).$$

3.2.3. Conservation of energy

For two-dimensional incompressible flow with mass flux through the leading- and trailing-edge boundaries, conservation of energy within the deforming control volume may be expressed

$$\left(\frac{\partial}{\partial t} - \frac{\partial}{\partial \theta}\right)\left(\frac{1}{2}v^2\frac{\partial V}{\partial \theta}\right) + \left(p_{le} + \frac{1}{2}v_{le}^2 - L_r\right)(\boldsymbol{v}_{r,le}\cdot\boldsymbol{n}_{le})\frac{\partial s_{le}}{\partial \theta} + \left(p_{te} + \frac{1}{2}v_{te}^2\right)(\boldsymbol{v}_{r,te}\cdot\boldsymbol{n}_{te})\frac{\partial s_{te}}{\partial \theta} = -\frac{\partial \boldsymbol{F}}{\partial \theta}\cdot\boldsymbol{v}_{cv}, \tag{3}$$

where the velocity of the control volume is approximated by the average of the velocities of the leading- and trailing-edge boundaries

$$\boldsymbol{v}_{cv} = \left(\frac{\partial}{\partial t} - \frac{\partial}{\partial \theta}\right)\left(\frac{x_{le} + x_{te}}{2}\boldsymbol{i} + \frac{\theta_{le} + \theta_{te}}{2}\boldsymbol{j}\right) + \boldsymbol{j}.$$

3.2.4. Blade dynamics

The blade dynamics are modelled using the typical section approach [Theodorsen (1935)]. The aerodynamic force which is coupled to the flow quantities through the momentum and energy conservation equations acts at aerodynamic center (assumed to be fixed at one-quarter chord length downstream from the leading edge). The blade plunge and twist are modelled as a pair of single degree of freedom oscillators with coupling through the inertia matrix. The inertial coupling vanishes when the elastic axis and center of gravity are coincident. The aerodynamic moment vanishes when the aerodynamic center and the elastic axis are coincident. Nominal values for the typical section parameters are extracted from a finite-element analysis of the first two vibration modes.

The blade bending and twist equations are as follows:

$$\left(\frac{\partial}{\partial t} - \frac{\partial}{\partial \theta}\right)^2 q + (\xi_{ea} - \xi_{cg})c\left(\frac{\partial}{\partial t} - \frac{\partial}{\partial \theta}\right)^2 \alpha + 2\zeta_b Q_b\left(\frac{\partial}{\partial t} - \frac{\partial}{\partial \theta}\right)q + Q_b^2 q = \frac{F_l}{D}, \tag{4}$$

$$\left(\frac{\partial}{\partial t} - \frac{\partial}{\partial \theta}\right)^2 \alpha + \frac{(\xi_{ea} - \xi_{cg})cD}{I_{ea}}\left(\frac{\partial}{\partial t} - \frac{\partial}{\partial \theta}\right)^2 q + 2\zeta_t Q_t\left(\frac{\partial}{\partial t} - \frac{\partial}{\partial \theta}\right)\alpha + Q_t^2\alpha = \frac{M}{I_{ea}}, \tag{5}$$

where

$$F_l = [\boldsymbol{F}(\theta + \pi/N_b, t) - \boldsymbol{F}(\theta - \pi/N_b, t)][-\sin(\gamma_r - \alpha)\boldsymbol{i} + \cos(\gamma_r - \alpha)\boldsymbol{j}],$$

$$M = F_l(\xi_{ea} - \xi_{cp})c$$

and

$$I_{ea} = D(\xi_{ea} - \xi_{cg})^2 c^2 + Dc^2\varepsilon^2.$$

3.2.5. Kinematic constraint

For closure, it is necessary to assume that the exit flow angle is fixed by the metal angle of the deflected blade plus some deviation

$$\frac{v_{2a} - (\frac{\partial}{\partial t} - \frac{\partial}{\partial \theta})\theta_{te}}{\phi_{2a} - (\frac{\partial}{\partial t} - \frac{\partial}{\partial \theta})x_{te}} = \tan(\beta_r - \alpha + \Delta), \tag{6}$$

where β_r is the metal angle of the trailing edge and the deviation Δ is assumed to be a linear function of the incidence angle

$$\Delta = \Delta_1\alpha_{\mathrm{inc},r} + \Delta_2.$$

The flow velocity relative to the leading edge, $\boldsymbol{v}_{r,le}$, has been defined previously. The incidence angle is then the difference between the flow angle and the leading-edge metal angle

$$\alpha_{\mathrm{inc},r} = \tan^{-1}\left(\frac{\boldsymbol{v}_{r,le}\cdot\boldsymbol{j}}{\boldsymbol{v}_{r,le}\cdot\boldsymbol{i}}\right) - \beta_{zr} + \alpha,$$

where β_{zr} is the zero incidence angle of the undeflected blade. The flow geometry is sketched in Fig. 5.

3.2.6. Lagged loss

The loss across the rotor bladerow, L_r, appears in the equation for energy conservation (3). As discussed in the previous section, the flow deviation from the trailing edge is assumed small and proportional to the incidence angle. The ideal pressure rise across the bladerow under steady conditions may then be determined using the Euler turbine equation. The difference between this ideal pressure rise and the measured pressure rise is the steady loss. Assuming that loss is a function of incidence angle only, the measured values can be fit well with a quadratic polynomial,

$$L_{r,qs} = L_{r1}\alpha_{\mathrm{inc},r}^2 + L_{r2}\alpha_{\mathrm{inc},r} + L_{r3}.$$

Thus, the model is "tuned" to match the steady performance of the experimental test rig. A first-order lag equation is used to model the fact that the time-dependent losses do not instantly equilibrate to changes in local incidence,

$$\left(\frac{\partial}{\partial t} - \frac{\partial}{\partial \theta}\right) L_r = -\frac{1}{\tau}(L_r - L_{r,qs}). \tag{7}$$

The time constant is chosen consistent with the blade passage convection time.

Eqs. (1), (3)–(7) and the two components of Eq. (2) are used to relate the exit flow quantities, ϕ_{2a}, v_{2a}, and p_{2a}, the blade deformation, α and q, the aerodynamic force, $\boldsymbol{F}$, and the loss, L, to the upstream flow quantities ϕ_1, v_1, and p_1. Each of these field quantities is projected over a finite number of Fourier components in the azimuthal variable. In the case of blade twist for example,

$$\alpha(\theta, t) = \alpha_1(t) + \sum_{n=1}^{N} \alpha_{2n}(t)\cos(n\theta) - \alpha_{2n+1}(t)\sin(n\theta).$$

A time-dependent system of differential algebraic equations is then derived through Galerkin projection of Eqs. (1)–(7) over the Fourier modes. From the Nyquist criterion, the number of Fourier modes required is equal to half the number of blades in the rotor.

3.3. Inter-bladerow gap

In the inter-bladerow gap, the azimuthal dependence of the flow is again modelled as a linear perturbation to the nominal axisymmetric flow. The perturbation to the axisymmetric flow is modelled as vortical, incompressible, inviscid flow. Inviscid flow implies that the vorticity is simply convected downstream. The perturbation velocity and pressure fields at the upstream and downstream ends of the inter-bladerow duct will be related to each other through the streamfunction and the associated vorticity.

The convection of vorticity implies a delay equation. In the present work, the convective delay is approximated with a first-order lag equation. The streamfunction is then determined and used to provide a mapping between the upstream and downstream pressures and velocities.

3.4. Stator (exit guide vanes)

The same fundamental equations of mass, momentum, and energy conservation apply equally to the stator as to the rotor. In the case of the stator, however, the vanes are assumed to be rigid thus the control volume does not deform. The conservation equations simplify immensely. Conservation of mass implies that axial components of velocity at the stator leading edge and trailing edges must be equal. The energy and axial momentum conservation equations are equivalent and reduce to the Bernoulli turbine equation. As in the case of the rotor, the steady losses are identified from data and a first-order lag equation is used to model the fact that the losses do not instantly equilibrate to changes in local incidence.

The exit guide vanes are designed for an exit flow angle of zero. The flow deviation at the vane trailing edge is neglected hence the trailing-edge azimuthal velocity is zero. This is a simplifying assumption rather than a necessary assumption.

3.5. Exit duct

In the exit duct, the azimuthal dependence of the flow is again modelled as a linear perturbation to the nominal axisymmetric flow. The nominal flow leaving the fan is a uniform jet.

With respect to flow perturbations, the flow in the exit duct is assumed to be incompressible and rotational. As mentioned previously the exit flow angle from the stator is zero; hence there is no azimuthal velocity at the stator trailing edge. The duct length is assumed infinitely long thus the flow perturbations decay exponentially downstream from the stator.

4. Results

4.1. Comparison of model and experiment

For parameters consistent with the test facility, the model gives very reasonable predictions of damping for flutter and stall. The model is "tuned" by choosing the losses as quadratic functions of the angle of attack to match the 9000 r.p.m. speedline of the test facility. The extent to which the predictions match other speeds is a measure of model robustness.

From a performance perspective, our interest is in stability boundaries on the operability map. Remarkably, these stability boundaries are found to be in good qualitative agreement with typical experience. Fig. 6 is a plot of the predicted stall and flutter stability boundaries on the operating map. A representative speedline corresponding to 9000 r.p.m. and the points at which flutter stability data have been acquired are indicated as well.

It is necessary to prescribe the structural damping parameter in order to match the average measured flutter damping across all nodal diameters. All other parameters are determined from the rig and blade geometry or are chosen by engineering judgement.

The most fundamental stability result is the relative stability of the flutter modes as a function of wave number (Fig. 7) and how the calculated values of damping vary with the operational parameters speed and flow (Fig. 8). Fig. 7 shows that the forward-travelling modes are least damped for this parameterization and that the zero and first-forward nodal diameter modes are most critical. Damping of all of the flutter modes decreases gradually with flow. Fig. 8 shows the dependence of damping of the critical flutter mode (nodal diameter 0) on flow as the exit flow area is varied for two different constant speeds. The damping trend with flow agrees well with the measured data but the model over-predicts the trend of damping with speed.

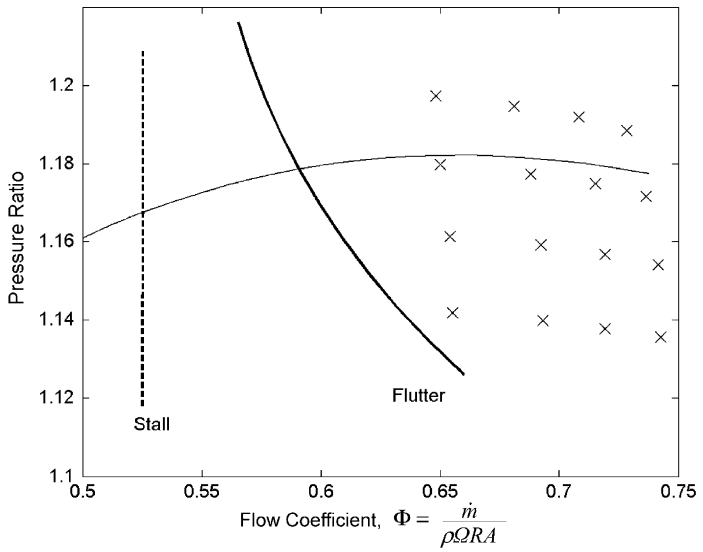

Fig. 6. Predicted flutter and stall stability boundaries on the operability map. This line corresponds to 9000 r.p.m. speedline. × 's correspond to points at which flutter damping has been measured.

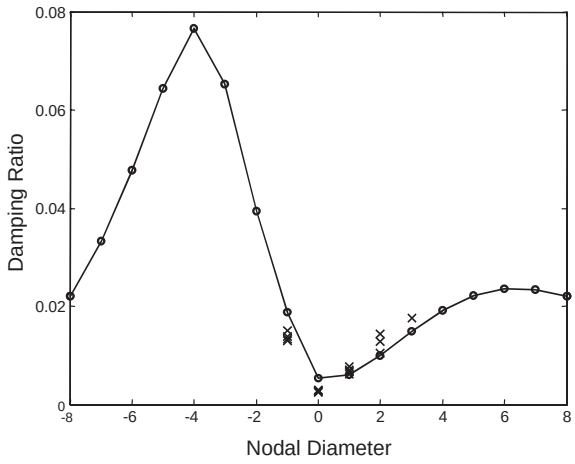

Fig. 7. Damping of all flutter modes by nodal diameter. Comparison of prediction to experiment, 9000 r.p.m. $\phi = 0.74$, PR = 1.17. $\times$'s correspond to points at which flutter damping has been measured. o's correspond to predictions.

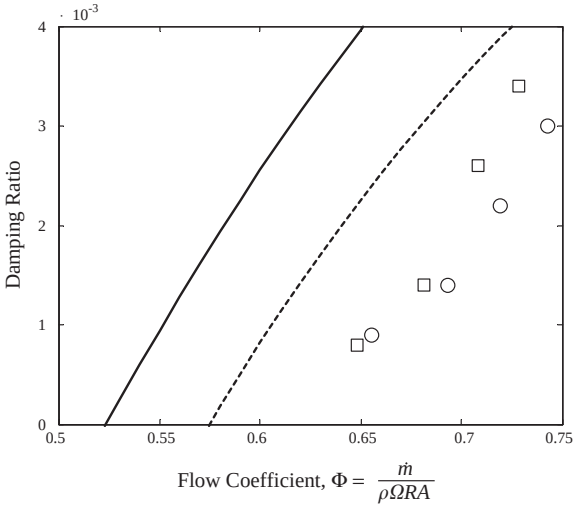

Fig. 8. Dependence of nodal diameter 0 flutter damping on speed and flow, comparison of prediction to measured values. 8000 r.p.m.: dashed line and circle markers, 9500 r.p.m.: solid line and square markers.

4.2. Parametric sensitivity

4.2.1. Sensitivity to natural frequency

Perhaps the first useful tool in engineering design for stall flutter avoidance was the development of experience-based flutter boundaries as functions of reduced velocity and rotor incidence angle. It is intuitive that higher incidence angles would be required to trigger flutter as the blades become effectively stiffer. These boundaries were found to be reliable across a "family" of similar blade designs under similar test conditions. The present model reflects this time-tested observation. The flutter boundary as a function of reduced velocity and incidence angle is plotted in Fig. 9. These points were computed by scaling the bending and torsional stiffnesses uniformly while holding all other parameters constant.

4.2.2. Sensitivity to plunge-to-twist ratio

Among the parameters most influential to flutter damping are those that govern the plunge-to-twist ratio of the blade deformation eigenmodes. In Fig. 10, the influence of plunge-to-twist ratio on flutter damping is examined. The ratio of

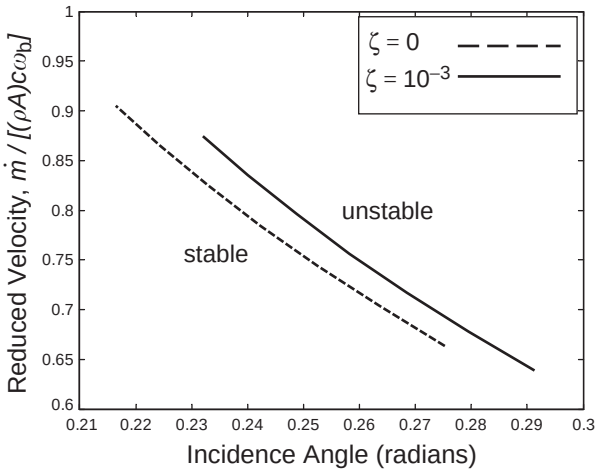

Fig. 9. Flutter boundary as a function of reduced velocity and rotor incidence angle. Also plotted is the contour for damping ratio of 10^{-3}.

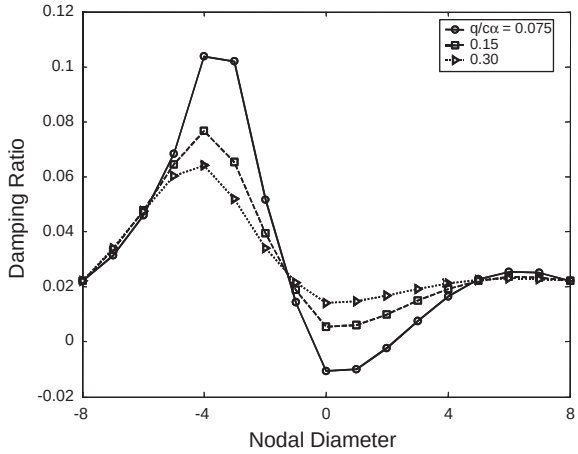

Fig. 10. Flutter damping by nodal diameter as blade plunge-to-twist ratio is varied from 0.075 to 0.3.

plunge-to-twist was varied by simultaneously adjusting the offset of the elastic axis from the center of gravity and the torsion and plunge stiffnesses in order to maintain the nondimensional natural frequencies. The impact on flutter damping is profound and suggests that mode shape "tailoring" may be an extremely fruitful direction of research even though the fundamental vibration mode shapes are strongly constrained by considerations of aerodynamic performance, cost, and weight.

4.2.3. Mistuning benefit

Fig. 11 contrasts the predicted effects of stagger and stiffness mistuning. Consistent with the previous literature, it is found that very modest alternate-blade stiffness mistuning is predicted to provide significant benefit to flutter damping (Crawley and Hall (1985); Bendiksen (1986); Shapiro (1998). In contrast, alternate-blade stagger mistuning is predicted to be weakly de-stabilizing. Aerodynamic mistuning has, in general, received far less attention in the literature (Bendiksen 1986). It is evaluated here in order to invalidate the supposition that moderate asymmetry of any sort is necessarily beneficial.

A consequence of mistuning is that the steady state solution is no longer axisymmetric nor are the system eigenmodes associated with any single Fourier harmonic. Of course, mistuning of sufficient magnitude will generate small length-scale disturbances pushing the limits of model validity.

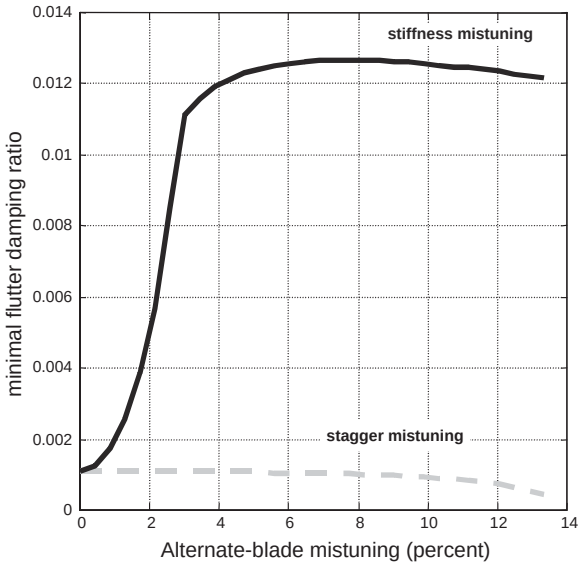

Fig. 11. Comparison of alternate-blade stiffness and stagger mistuning.

In order to verify the efficacy of alternate-blade stiffness mistuning, as opposed to improvement simply from a shift in the average frequency, three experimental configurations were tested: the baseline rotor with flexible blades, a rotor with stiff blades, and a rotor with alternate flexible and stiff blades. At speed, the blade vibration frequencies of the flexible and stiff blades are 23% lower and 23% higher than the average frequency. In the case of the all-flexible and all-stiff configurations, the flutter modes were clearly evident in power spectra of blade deflection and strain gage data. For the mistuned disk, flutter was undetectable at all operating points. Practical limitations prevented considering a case with a more modest level of mistuning.

Experimentally determined speedlines for the flexible, mistuned, and stiff disks are shown below in Fig. 12. For the flexible disk configuration, operability was limited by high-incidence flutter in the first bending mode in a zero nodal diameter pattern (ND0). The forward-travelling first nodal diameter mode (ND1 +) was also very lightly damped. In contrast, the operability for the stiff and mistuned configurations was limited by rotating stall only; flutter was not detected any where in this operating range.

Spectral analysis of blade deflection and strain for the configuration with flexible blades and for the configuration with stiff blades revealed sharp peaks corresponding to the least damped flutter modes. In contrast, there were no peaks evident in the spectra for the alternating-stiffness disk other than multiples of the shaft frequency. A comparison of power spectral densities of root leading-edge strain for one of the flexible blades between the all-flexible configuration and the alternating flexible-stiff configuration is shown in Fig. 13. Note that the two flutter modes (ND0 and ND1 +) clearly stand out from the broad peak at 250 Hz. This is a typical for rotor-frame measurements. Blade deflection measurements from the same tests are presented in Fig. 14. These measurements are relative to the stator frame, which helps in the interpretation by clearly separating the travelling wave modes. System identification of the two flutter modes yielded a natural frequency of 273 Hz and damping ratio of 0.89×10^{-3} for the ND0 mode and a frequency of 407 Hz and (rotor frame) and damping ratio of 1.35×10^{-3} for the ND1 + mode. The disk of stiff blades likewise exhibited clear flutter peaks but they are much more damped than the flutter modes of the flexible disk. The lowest measured flutter damping ratio was 2.70×10^{-3} for the ND0 mode, which was at 440 Hz. The mistuned disk did not have any clear flutter modes. The broad-band response around 400 Hz (Fig. 14, lower plot) was swept with nodal diameters 0, 1, 2 and 3 forcing but no travelling wave response could be elicited.

A mental picture for the beneficial effect of alternating-stiffness mistuning is that for disturbances at either frequency, every other blade is effectively unmoving. It is as if each blade is oscillating in a fixed channel.

Figs. 15 and 16 summarize the measured effects of alternate stagger mistuning on flutter damping. In these experiments the stagger angle varies 6.7% from nominal alternately up and down. Fig. 15 shows the flutter stability boundaries for the "tuned" (baseline) case and the mistuned case. Measured on five different speedlines, the flutter

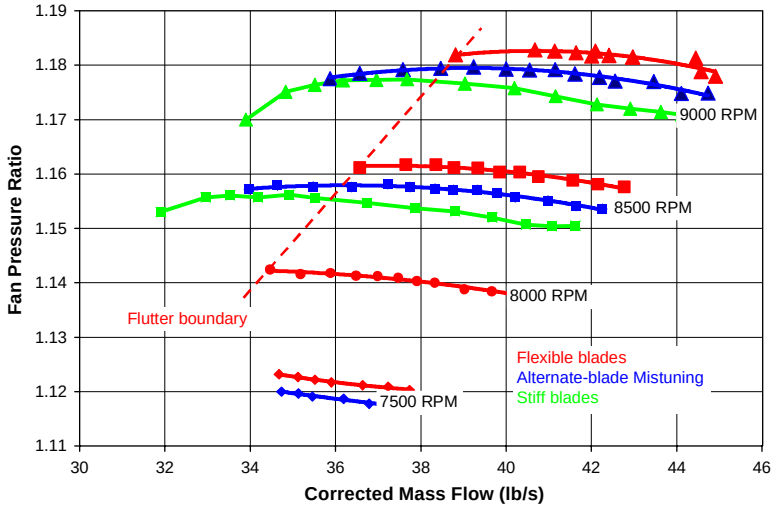

Fig. 12. Speedlines showing flutter boundaries for three configurations: all flexible blades, alternate-blade stiffness mistuning, and all stiff blades.

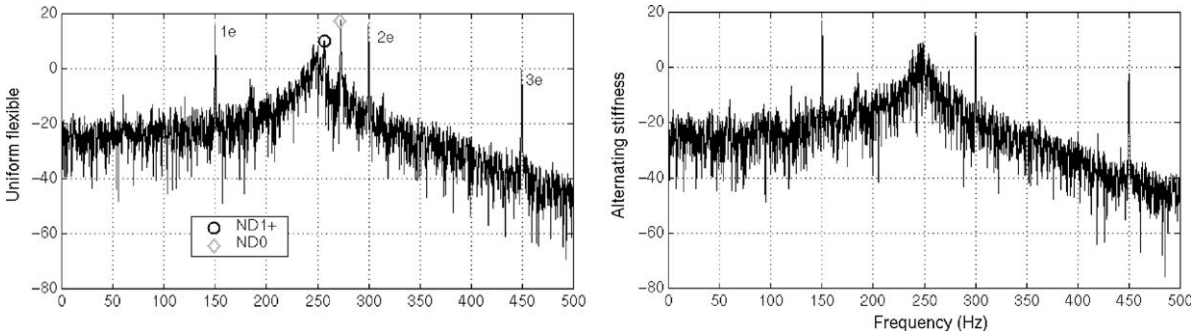

Fig. 13. Power spectra of root-leading edge strain, same blade, for tuned (flexible) configuration and for alternate-blade stiffness mistuning.

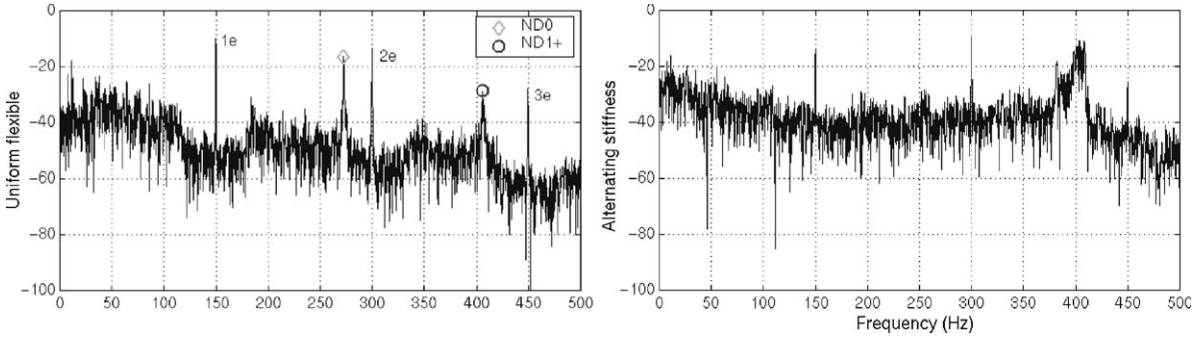

Fig. 14. Power spectra of blade deflection for tuned (flexible) configuration and for alternate-blade stiffness mistuning.

boundary for the alternate-stagger mistuning configuration is encountered at lower pressure ratios than in the baseline case. The stability-limiting flutter mode in all cases is ND0. The flutter damping for multiple nodal diameters are compared in Fig. 16.

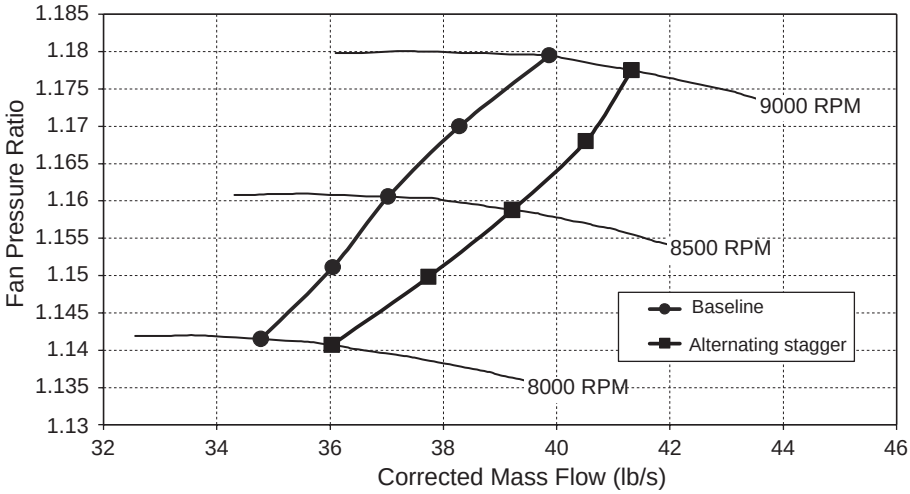

Fig. 15. Flutter boundaries for "tuned" and alternate-stagger mistuning configurations.

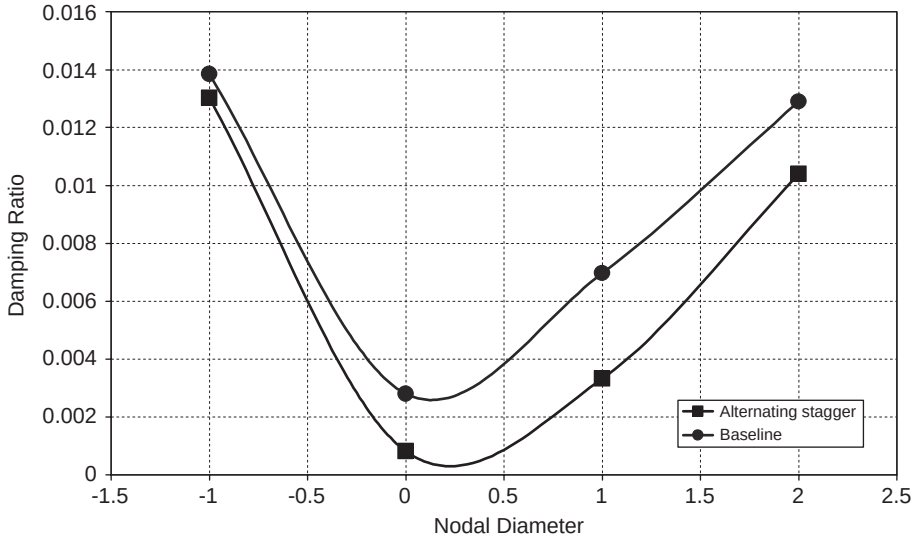

Fig. 16. Relative damping of flutter modes by nodal diameter. Comparison of "tuned" and alternate-stagger mistuning.

5. Conclusion

The present results demonstrate that actuator disk models have good predictive capability for trends in flutter stability when appropriately parameterized to match the over-all performance (pressure rise as a function of flow). Furthermore, these models have been exercised to evaluate parameter sensitivity that would be quite difficult to evaluate through testing or higher-fidelity modelling.

The model is relatively low dimensional and is suitable for development of active or passive control strategies. Such models may ultimately be useful for on-engine diagnostics or control.

Acknowledgements

This work was supported by the Air Force Office of Scientific Research under contract F49620-95-C-0035. Marc Q. Jacobs was the program manager.

Dan Gysling and Mark Myers developed the first incarnation of the model and were a driving force in development of the project. Their fundamental vision for the model is still intact. The modelling effort benefited further from conversations with Gavin Hendricks, Joe Verdon, Matthew Feulner, Edward Greitzer, James Paduano and Maverick Wong.

The authors are particularly indebted to Karen Teerlinck, test engineer for the UTRC main wind tunnel, and an excellent crew of technicians.

References

Banaszuk, A., Gysling, D., Rey, G., 2002. Active control of flutter in turbomachinery using off blade actuators and sensors. In: 15th International Federation of Automatic Control World Congress, Barcelona, Spain, July 21–26, 2002.

Bendiksen, O.O., 1986. Recent developments in flutter suppression techniques for turbomachinery rotors. AIAA Journal of Propulsion and Power 4 (12), 167–171.

Copeland, G.S., 1997. Reduced-order DAE models for turbomachinery stall, surge, and flutter. In: Annual Meeting of the Gesellschaft für Angewandte Mathematik und Mechanik, March 24–27, Regensburg, Germany.

Copeland, G.S., Rey, G.J., 1998. Nonlinear modeling, analysis, and control of turbomachinery stall flutter. AFOSR Technical Report, contract number F49620-95-C0035.

Crawley, E.F., Hall, K.C., 1985. Optimization and mechanisms of mistuning in cascades. ASME Journal of Engineering for Gas Turbines and Power 107, 418–426.

Gysling, D.L., Myers, M.R., 1996. A framework for analyzing the dynamics of flexibly-bladed turbomachines. ASME 96-GT-440. International Gas Turbine and Aeroengine Congress and Exhibition, Birmingham, UK, June 10–13, 1996.

Moore, F.K., Greitzer, E.M., 1986. A theory of post-stall transients in axial compression systems: Parts I and II. ASME Journal of Engineering for Gas Turbines and Power 108, 231–239.

Shapiro, B., 1998. A symmetry approach to extension of flutter boundaries via mistuning. AIAA Journal of Propulsion and Power 14 (3), 354–366.

Silkowski, P.D., Rhie, C.M., Copeland, G.S., Eley, J.M., Bleeg, J.A., 2002. Computational fluid dynamics investigation of aeromechanics. AIAA Journal of Propulsion and Power 18 (4), 788–796.

Theodorsen, T., 1935. General theory of aerodynamic instability and the mechanism of flutter. NACA Report 496.

Whitehead, D.S., 1987. Classical Two-Dimensional Methods, AGARD Manual on Aeroelasticity in Axial-Flow Turbomachines, Vol. 1. AGARD-AG-298 (Chapter 3).

Wong, M.T.M., 1997. System modeling and control studies of flutter in turbomachinery. M.S. Thesis, Massachusetts Institute of Technology, Cambridge, MA, USA.